









RESEARCH ARTICLE | FEBRUARY 09 2024

Polymeric liquids in mesoporous photonic structures: From precursor film spreading to imbibition dynamics at the nanoscale

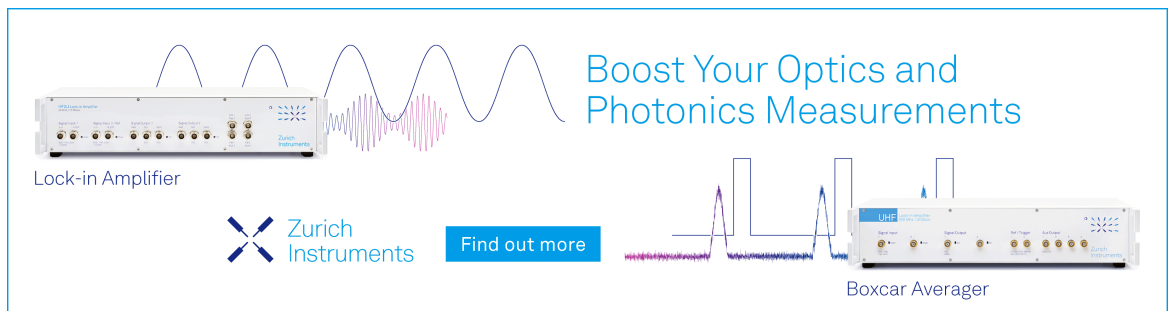
Special Collection: [Polymer Nanoconfinement](#)

Guido Dittrich ; Luisa G. Cencha ; Martin Steinhart ; Ralf B. Wehrspohn ; Claudio L. A. Berli ; Raul Urteaga ; Patrick Huber  




J. Chem. Phys. 160, 064903 (2024)

<https://doi.org/10.1063/5.0189633>



Boost Your Optics and
Photonics Measurements

Lock-in Amplifier

 Zurich
Instruments

[Find out more](#)

Boxcar Averager

Polymeric liquids in mesoporous photonic structures: From precursor film spreading to imbibition dynamics at the nanoscale

Cite as: J. Chem. Phys. 160, 064903 (2024); doi: 10.1063/5.0189633

Submitted: 30 November 2023 • Accepted: 11 January 2024 •

Published Online: 9 February 2024



View Online



Export Citation



CrossMark

Guido Dittrich,¹ Luisa G. Cencha,² Martin Steinhart,³ Ralf B. Wehrspohn,^{4,5} Claudio L. A. Berli,⁶
Raul Urteaga,² and Patrick Huber^{1,7,a)}

AFFILIATIONS

¹Institute for Materials and X-Ray Physics, Hamburg University of Technology, 21073 Hamburg-Harburg, Germany

²IFIS-Litoral (Universidad Nacional del Litoral-CONICET), Guemes 3450, 3000 Santa Fe, Argentina

³Institute of Chemistry of New Materials, Osnabrück University, 49076 Osnabrück, Germany

⁴Institute of Physics, Martin Luther University of Halle-Wittenberg, 06120 Halle (Saale), Germany

⁵Korea Institute of Energy Technology (KENTECH), 21 Kentech-gil, Naju 58330, South Korea

⁶INTEC (Universidad Nacional del Litoral-CONICET), Predio CCT CONICET Santa Fe, RN 168, 3000 Santa Fe, Argentina

⁷Center for X-Ray and Nano Science CXNS, Deutsches Elektronen-Synchrotron DESY, 22603 Hamburg, Germany

Note: This paper is part of the JCP Special Topic on Polymer Nanoconfinement.

^{a)}Author to whom correspondence should be addressed: patrick.huber@tuhh.de

ABSTRACT

Polymers are known to wet nanopores with high surface energy through an atomically thin precursor film followed by slower capillary filling. We present here light interference spectroscopy using a mesoporous membrane-based chip that allows us to observe the dynamics of these phenomena *in situ* down to the sub-nanometer scale at milli- to microsecond temporal resolution. The device consists of a mesoporous silicon film (average pore size 6 nm) with an integrated photonic crystal, which permits to simultaneously measure the phase shift of thin film interference and the resonance of the photonic crystal upon imbibition. For a styrene dimer, we find a flat fluid front without a precursor film, while the pentamer forms an expanding molecular thin film moving in front of the menisci of the capillary filling. These different behaviors are attributed to a significantly faster pore-surface diffusion compared to the imbibition dynamics for the pentamer and vice versa for the dimer. In addition, both oligomers exhibit anomalously slow imbibition dynamics, which could be explained by apparent viscosities of six and eleven times the bulk value, respectively. However, a more consistent description of the dynamics is achieved by a constriction model that emphasizes the increasing importance of local undulations in the pore radius with the molecular size and includes a sub-nanometer hydrodynamic dead, immobile zone at the pore wall but otherwise uses bulk fluid parameters. Overall, our study illustrates that interferometric, opto-fluidic experiments with mesoporous media allow for a remarkably detailed exploration of the nano-rheology of polymeric liquids.

© 2024 Author(s). All article content, except where otherwise noted, is licensed under a Creative Commons Attribution (CC BY) license (<http://creativecommons.org/licenses/by/4.0/>). <https://doi.org/10.1063/5.0189633>

I. INTRODUCTION

Polymeric liquids exhibit a variety of transport mechanisms during capillary filling of mesoporous materials. Understanding them is essential for many applications. For example, immobile layers at the pore walls or confinement effects are important for separation processes^{1,2} and the formation of precursor films can be used for templated tubes³ and temperature-dependent imbibition for passive temperature sensors,⁴ to just name a few.

Discussions describing capillary rise in nanopores often start with the Lucas–Washburn equation.^{5,6} It relates the driving capillary pressure to the counteracting viscous drag in a \sqrt{t} vs imbibition length L dependency. Although it is not suitable to solve every capillary filling problem, in particular if there are systematic variations in the hydraulic permeability,⁷ it is fairly close to many solutions of more complex porous systems and liquids.^{8–10} The prefactor of the Lucas–Washburn equation can be divided into (1) fluid-centered

properties, surface tension σ , viscosity μ , and the liquid–solid contact angle θ , and (2) geometrical properties, an effective pore radius r_{eff} whose definition captures the nature of the porous structure,

$$L(t) = \Gamma \sqrt{r_{\text{eff}} t}, \quad (1)$$

where $\Gamma = \sqrt{\frac{\sigma \cos \theta}{2\mu}}$.

Many experimental studies have been performed on melt infiltration of polymers, with a molecular weight above the critical value (M_c) for entanglements, into nanopores.^{11–14} In such studies^{11,12} on melt infiltration of polystyrene into anodized aluminum oxide with straight pores and into the sponge-like structure of controlled porous glass, a square-root-of-time law was used to model the dynamics. Pearson correlation coefficients for different exponents of a power-law fit suggested though an even better fit for exponents deviating from the famous Lucas–Washburn equation like \sqrt{t} proportionality.

The authors of the work of Yao *et al.*¹⁵ proposed a unified theory of capillary rise dynamics of polymers $>M_c$ involving an immobile layer and reptation under pressure model. The latter explains the relative increase of imbibition dynamics with molecular mass, in contrast to the increasing bulk viscosity, by disentanglement under confinement. In the immobile layer model, the pore radius behind the imbibition front is reduced by adsorbed molecules. This phenomenon is also observed for polymeric liquids with molecular weight below M_c and other liquids.

Polymeric liquids below M_c under confinement exhibit imbibition phenomena that are not well understood yet. Predictions of a molecular dynamics simulation of Lennard-Jones (LJ) fluids and a decane melt in a cylindrical nanopore are in close agreement with the Lucas–Washburn predictions.¹⁶ In the case of slip flow, they suggest modifying the Lucas–Washburn equation by virtually increasing the radius by a slip length. Moreover, a much faster precursor film spreading obeying a square-root-of-time law has been inferred in atomistic simulations.¹⁷

Engel and Stühn¹⁸ studied polyisobutylene and poly- ϵ -caprolactone in mesoporous polycarbonate (both $<M_c$) by *in situ* small angle x-ray scattering. They found a fast first wetting of the pore walls by a precursor film, followed by a much slower than expected complete filling. The fast initial wetting is attributed to a stronger adhesive than cohesive force. Although the aspect ratio of pore size to the radius of gyration was not small at all, they discovered a strong confinement effect on complete filling.

In situ nanodielectric spectroscopy is simultaneously sensitive to molecular dynamics and capillary rise. An imbibition study¹⁹ on *cis*-polyisoprene ($<M_c$) in anodized aluminum oxide (AAO) has measured two-time regimes decelerated compared to the Lucas–Washburn equation. An increasing molecule–wall interaction with time for native AAO was concluded, as less freely fluctuating chains were contributing to the dielectric signal. Modifying the surface by silanization successfully reduced the interaction.

Recent single-pore molecular dynamics simulations of LJ fluids predict slower capillary filling for short polymer chains, below M_c for entanglements, compared to the Lucas–Washburn prediction, while longer chains show the opposite trend.²⁰ The slowed down filling dynamics of short polymer chains is explained by a nearly immobile layer with finite slip and lower free energy due to confinement. It is quantified by an effective viscosity, which is twice the bulk

viscosity for a radius-to-chain length ratio of one and, interestingly, increases for higher ratios.

We focus here on the imbibition dynamics of styrene oligomers in mesoporous silicon and will see that our observation fit such a slowdown seen in the simulations. Moreover, we are going to scrutinize the relevance of precursor film spreading for the imbibition phenomenology.

Mesoporous silicon (pSi) is an established functional material,^{21–25} most prominently used in optical sensing applications for biochemistry,²⁶ gases,²⁷ and fluid dynamics.²⁸ It can also be used to explore the effect of nanoconfinement on condensed matter^{10,29–32} or the mechanical properties of a mainstream mesoporous semiconductor.^{33,34} A common optical sensing mechanism relies on change of the effective refractive index of porous layers during the displacement of air by an analyte. Porous silicon is electrochemically etched in a self-organizing top-down process with a strong anisotropy of the pores in the etching direction. When the pore size and interpore distances are much smaller than the probing wavelength of an electromagnetic wave, the effective optical properties of pSi are adjustable by the porosity and thickness. The latter parameters depend on the synthesis conditions. Continuous or abrupt changes in the in-depth porosity can be accomplished by the course of applied current density, whereas the time applied determines the thickness. This enables the synthesis of layered structures, Bragg- and Rugate-filters, as well as 1D photonic crystals.²⁶ These structures can be applied for *in situ* investigation of polymer infiltration into mesoporous scaffold materials,²⁸ providing an improved resolution in the plane perpendicular to the pore orientation.

II. PROBLEM STATEMENT

It has been demonstrated that *in situ* white light reflection spectroscopy of pSi photonic crystals (PC) provides the precision to resolve precursor film spreading. A thin film pSi layer in front of the PC [Figs. 1(a) and 1(b)] acts as a column to investigate different imbibition lengths and, thereby, times. The shape of fluid fronts can be inferred from rescaling the filling dynamics of the PC with a capillary filling model for the fluid transport of the in-front homogeneous porous layer.²⁸

As outlined above, polymers exhibit a variety of different dynamics for the infiltration of mesoporous scaffolds,¹⁵ depending on the molecular weight, temperature, entanglements, shear thinning/thickening³⁵ behavior, or confinement. Therefore, the capillary filling model that best fits the experimental data needs to be adapted for each fluid. The geometrical descriptor of the scaffold imbibed should on the contrary be unanimous.

In the following, a method is introduced, where the infiltration of the stacked pSi layer (thin film + PC) is measured simultaneously with two spectrometers comprising two different wavelength ranges: visible and near-infrared (NIR). In this way, the infiltration curve corresponding to the PC can be decoupled from the infiltration curve of the stacked layer. Both curves, combined, allow us to infer not only the meniscus dynamics but also the precursor film profile and dynamics. In this study, we have used two oligostyrenes as imbibition fluids. Overall, we employed a previously reported high-precision technique²⁸ to test a simple model based on the presence of a dead layer in corrugated tubes to explain the dynamics of

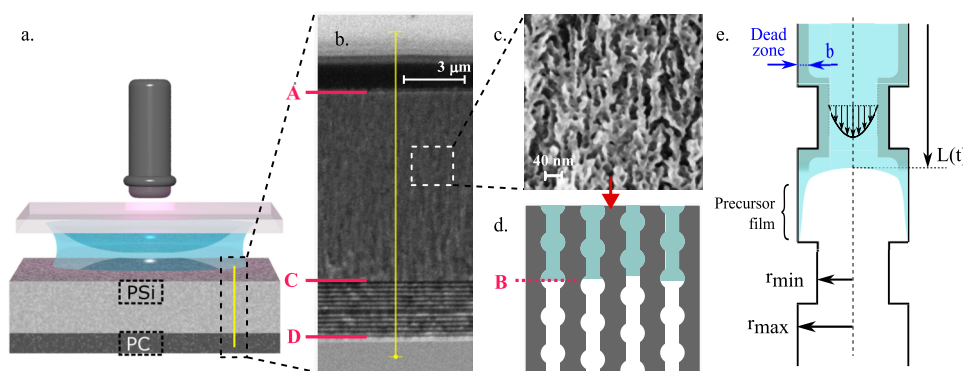


FIG. 1. (a) Illustration of the measurement setup, starting from the top consisting of a reflection probe, glass carrier, oligomer film, and sample. (b) Scanning electron micrograph of the sample regions indicated in the illustration. The optical interfaces are indicated by capital letters A, C, and D. Interface A is between air and pSi thin film, C is between the thin film and PC, and D is between the PC and the crystalline Si substrate. (c) PSi structure with a strong anisotropic pore orientation in the direction of the etching although the displayed pore walls on the given scale appear dendritic. (d) Simplified representation by a constriction model. The moving fluid front is indicated by capital letter B. (e) Single representative, constricted tube with a dead zone for the fluid velocity profile during spontaneous imbibition.

these oligomers under conditions of high spatial confinement. This holds particular relevance for understanding polymer infiltration into nano- and mesopores.

III. MATERIALS

Probing liquids are monodisperse oligostyrenes (OSs) (from Polymer Standards Service) with two (OS-2) and five (OS-5) monomer repetition units, having a sec-butyl and proton end group. Because of their well-defined properties, OS molecules are commonly used as a standard for gel-chromatography. The viscosity at room temperature is analyzed by a rheometer (Kinexus Prime Series) in plate-to-plate geometry, resulting in a viscosity of $34\,000 \pm 570$ mPas in a shear-rate range of 0.01–100 Hz and 9.4 ± 2.1 mPas at 100–51 600 Hz for OS-5 and OS-2, respectively. Both liquids provide Newtonian fluid behavior in the shear-rate range of the capillary filling. Other parameters of interest in the analysis include the surface tension (σ) with a value of 40.7 mJ/m²³⁶ and a contact angle cosine of $\cos \theta = 1.37$. The optical parameters utilized for the RIFTS assessment of porosity and thickness include the refractive indexes for crystalline silicon, air, and oligostyrenes. These indexes, corresponding to mean values between 1150 and 1650 nm, are as follows: $n_{\text{Si}} = 3.51$,³⁸ $n_{\text{air}} = 1$,³⁹ and $n_{\text{OS}} = 1.57$,⁴⁰ respectively. Additionally, a mean hydraulic radius of $r_h = 5.8$ nm was employed.²⁸

Porous silicon is fabricated by electrochemical anodization. Monocrystalline 100-orientation, boron doped (p-type) wafers with resistivity of 1–4 m Ω cm are treated with a HF(50 wt. %):EtOH 1:2 volumetric solution and different current densities. By variation of the latter, layers with different thicknesses and porosity can be obtained. For the current method, a thin film layer of largely homogeneous porosity is etched first, subsequently followed by a PC. The PC is designed with its bandgap and width in the visible range, whereas the overall stack of the layers has a detectable interference pattern in the NIR range of the used setup. The pSi thin films were fabricated using a current density of 12.7 mA cm⁻², while the PC was fabricated by alternating current densities of 12.7 and 50.9 mA cm⁻².

More information about the synthesis can be found in a previous publication.²⁸

IV. SETUP

Measurements are conducted with a white light reflection spectroscopy setup (Fig. 1) consisting of a glass fiber bundle reflection probe with 17 illumination and two read fibers. Illumination is provided by a balanced deuterium–halogen light source (AVALIGHT-DH-S-BAL) with a spectral range of 215–2500 nm. One read fiber is connected to an UV–Vis spectrometer (AvaSpec-2048CL) equipped with a 10 μm slit, of spectral range 200–1100 nm and spectral resolution 1 nm. The other is connected to an NIR-spectrometer (AVASPEC-NIR512) with a 25 μm slit, 850–1650 nm spectral range and a spectral resolution of 4 nm.

V. METHOD

The imbibition of oligostyrenes is monitored by *in situ* white light spectroscopy at normal incidence and conducted at room temperature. Before the experiment, pSi samples are cleaned with toluene and allowed to dry. The oligomers are drop-cast on a glass substrate and fixed in front of the reflection probe [see Fig. 1(a)]. Spontaneous capillary rise is initiated once the polymer film is brought in direct contact with the sample. The sampling rates of the spectrometers were chosen to be 500 ms for OS-5 and 1–5 ms for the lower viscosity OS-2, respectively.

At first, the pSi thin film is infiltrated. The substitution of air by OS with its higher refractive index increases the effective refractive index n_{eff} of the material, which can be measured by a proportional shift of the optical thickness (e) according to $e = 2d \cdot n_{\text{eff}}$, where d is the physical thickness. Assuming an endless supply of liquid during capillary filling, a normalized optical thickness $\Delta e(t)$ [Eq. (2)] can be determined by the values at the starting and completed filling time t_0 and t_{end} , respectively. This normalized optical thickness reflects the filling fraction of the imbibition. Equally valid, as the

wavelength for a given peak in the reflectance spectrum is proportional to the optical thickness at that time,⁴¹ one can follow along the normalized wavelength shift $\Delta\lambda(t) = (\lambda(t) - \lambda(t_0))/(\lambda(t_{\text{end}}) - \lambda(t_0))$ of an interference extremum in the spectrum, as this also reflects the change in optical thickness. In the case of homogeneous porosity, which implies a homogeneous n_{eff} , through the entire thickness, $\Delta e(t)$ is directly related to the imbibition fluid front position. For other pore morphologies, $\Delta e(t)$ accounts for the relative pore volume infiltrated. With the range of layer thicknesses between 3 and 20 μm , it was found that the optical thickness is determined with the best signal-to-noise ratio in the wavelength range of 1150–1650 nm.

For a single thin film, a simple sinusoidal interference pattern would be measured that undergoes a phase shift during capillary filling. This can be tracked by several methods.

The sinusoid interference pattern due to thin film comes from interference of light reflected at interfaces A and C [see Fig. 1(b)]. Note that the moving interface B, due to the liquid advancing front [Fig. 1(d)], does not contribute to interference since it reflects a negligible amount of light. This is because of its smaller contrast of refractive index at each side of the interface when compared with interfaces A and C and because the fluid front is not perfectly flat, which means part of the light is scattered. On the other hand, the PC will exhibit a marked peak at its resonance position λ_0 and its reflectance spectra will be given by the interference of reflection at interfaces C and D [Fig. 1(b)].

After moving through the thin film, the liquid reaches the PC, whose resonance position λ_0 strongly depends on the liquid filling fraction of its central defect, causing a shift of λ_0 and providing information of the liquid filling fraction at one specific location, after the thin film in this case. In this way, the joint information provided by the evolution of the thin film optical thickness and by the evolution of λ_0 can help elucidate the fluid front profile inside the porous structure.

Because of the stacked structure of pSi thin film and PC, a superposition of sinusoids is measured. A mathematical transformation method facilitates differentiating the sinusoids and attributing them to the respective physical layer. Therefore, a Hann-windowed fast Fourier transformation (FFT) is used for analysis of the optical thickness. This method is known as reflective interferometric Fourier transform spectroscopy (RIFTS).²¹ Figure 2 displays the FFT of an empty and subsequently OS-filled sample. The three most prominent peaks, indicated by vertical dotted lines, can be attributed to the PC, the thin film, and the stack of both from left to right. This is conducted by effective medium approximation with the orthogonal Maxwell Garnett model Eq. (3),⁴² where Φ_i is the average porosity of layer i , $n_{1/2}$ is the refractive index of the filling medium and n_{Si} that of silicon, in conjunction with $e_{\text{ot}} = 2d \cdot n_{\text{eff}}$.

The thickness values are in good agreement with those obtained by scanning electron microscopy and the porosities are consistent (Table I). An approach to measuring the capillary filling would be to follow the particular optical thickness peak in the FFT over time. This has been found challenging for the PC and thin film peak, as they are not always apparent, since the thin film peak is too close to the peak of the overall stack. Here, a major problem arises from windowing, which increases the width of the peaks but is also a necessity to reduce spectral leakage and, thereby, side lobes of the main peaks. The solution chosen is to follow the optical thickness of the stack

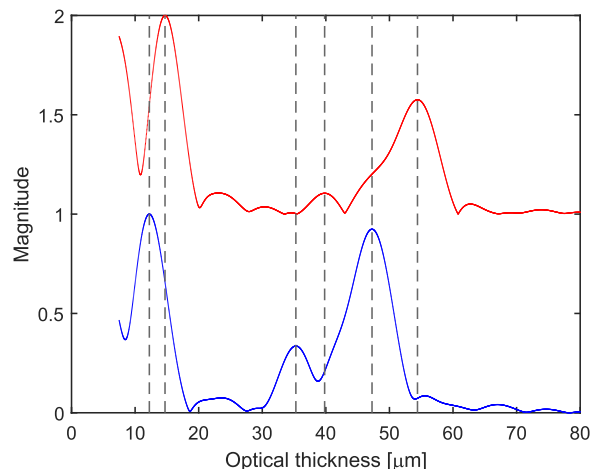


FIG. 2. Fast Fourier transform (FFT) of the initial (blue) and final (red) spectrum in the NIR region from 1150 to 1650 nm. For illustration purposes, the magnitude of the final curve is shifted by a magnitude of one. The dashed lines indicate the center of the main peaks by full width half maximum (FWHM) peak determination. Start and end position of the respective peaks are used to solve the orthogonal Maxwell–Garnett effective medium approximation [Eq. (3)] for the layers empty and filled state as described in this section. The layers' thickness and porosity are listed in Table I.

(see Fig. S2). An equivalent alternative technique is to follow the wavelength temporal evolution of a certain peak of the interference pattern in the spectrum, $\lambda_{\text{peak}}(t)$. In this method, the resulting data series is normalized by the initial and final wavelengths. The latter method requires less processing time and, because of that, is the chosen one in this work. A comparison of the curves obtained by both methods can be found in Fig. S2. We have

$$\Delta e(t) = \frac{e(t) - e(t_0)}{e(t_{\text{end}}) - e(t_0)}, \quad (2)$$

$$n_{1/2}^2 = \frac{\Phi_i \left(n_{1/2}^2 \frac{2n_{\text{Si}}^2}{n_{1/2}^2 + n_{\text{Si}}^2} - n_{\text{Si}}^2 \right) + n_{\text{Si}}^2}{\Phi_i \left(\frac{2n_{\text{Si}}^2}{n_{1/2}^2 + n_{\text{Si}}^2} - 1 \right) + 1}. \quad (3)$$

Subsequently, the PC is filled by the invading OS. Here, the filling of the central cavity can be measured by the increasing wavelength of its resonance valley.²⁸ It can be normalized to start and end analogously to the optical thickness in Eq. (2). Abstractly viewed, due to the characteristic intensity amplification in the cavity at the

TABLE I. Thickness d_{oMG} and porosity Φ_{oMG} by orthogonal MG using the RIFTS method²¹ for the measurement displayed in Fig. 2. The thickness is in reasonable agreement with SEM measurements and the equality $d_{\text{tot}}\Phi_{\text{tot}} = d_{\text{film}}\Phi_{\text{film}} + d_{\text{PC}}\Phi_{\text{PC}}$ is satisfied.

| Layer | d_{SEM} (μm) | d_{oMG} (μm) | Φ_{oMG} (%) |
|-----------|------------------------------------|------------------------------------|-------------------------|
| PC | 3.4 | 3.5 | 71 |
| Thin film | 9.3 | 8.3 | 55 |
| Stack | 12.7 | 11.9 | 61 |

resonance wavelength λ_0 , the optical microcavity works as a sensor for liquid filling at the particular position of the microcavity center. The resonance wavelength λ_0 is mainly determined by the optical thickness of the central defect. In turn, the optical thickness of this central porous layer depends on the liquid filling fraction, i.e., the relative proportion of liquid in the porous structure. This means that during imbibition, the resonance condition will shift to longer wavelengths only when the liquid reaches the central defect of the microcavity.

The porous silicon is effectively closed at the bottom. Therefore, imbibition could be delayed by the increasing pressure of the trapped air. This problem has been carefully studied in Refs. 13 and 41. Due to relatively high capillary pressure, the effect of air compression is negligible in almost the entire pore space, except in the last 5% of the sample, which is not reached in our measurements. The central region of the microcavity is at least 10% before the closed end of the sample. Moreover, for pSi membranes, the filling time is not affected by the trapped air compression.

VI. ANALYSIS

In the following, capillary rise in pSi is treated as its structure consists of an unconnected array of pores, which can be described by a representative effective pore radius r_{eff} . The dynamics of fluids for this kind of problem are often described or at least compared to the Lucas–Washburn equation. Since many studies of more complex liquids and geometries have discovered deviations from this law, several modified Lucas–Washburn equations like square-root-of-time laws have been proposed.

The authors of the work of Cencha *et al.*⁴³ have demonstrated that the melt infiltration of an ethyl vinyl acetate copolymer into pSi can be described by taking into account a mean hydraulic radius $\langle r_h \rangle = 2A/P$, defined by (1) the ratio of pore perimeter P and area of the cross section A and (2) a tortuosity parameter τ_L [Eq. (4)]. The latter is the elongation factor relating the imbibition length, i.e., the normal of the material's surface plane and the center of the imbibition front, to the actual path of a fluid through a meandering pore. In previous experiments with short chained alkanes, a value of 2.6 was determined for this tortuosity in pSi.⁴¹ We have

$$r_{\text{eff}} = \frac{\langle r_h \rangle}{\tau_L^2}. \quad (4)$$

In that approach, the concept of tortuosity comes to mathematically explain the abnormally low effective radius r_{eff} that is required to describe the experimental results. Actually, r_{eff} represents a straight cylindrical pore with the same imbibition dynamics. In the present work, we adopt a different strategy to describe the polymer infiltration in the mesoporous silicon: We start by defining a pore network that better represents the observed physical structure [Fig. 1(d)] and then incorporate corrections that compensate for some nanoscale effects, notably the presence of a stagnant polymer layer on the pore walls. Calculations are made in the framework of the sub-continuum approach,⁴⁴ where continuum equations are still valid, although emerging confinement effects are to be considered.

More precisely, we consider an array of nanotubes with periodic modulation of the cross-section, where the pore radius varies between r_{min} and r_{max} [Fig. 1(e)]. Then, momentum and mass conservation equations are applied to calculate the spontaneous

imbibition dynamics. Assuming that modulations randomly repeat along the tube, the effective radius can be written as

$$r_{\text{eff}} = \frac{1}{\langle r^{-4} \rangle \langle r^3 \rangle}, \quad (5)$$

where $\langle r^n \rangle = \frac{1}{h} \int_0^h r(z)^n dz$ is the n th probability moment of the radius distribution, h being the distance across the porous material.⁴⁵ It is worth noting that Eq. (5) had been previously reported, though, with a less general formalism.⁴⁶ In particular, for an array of tubes with periodic step changes of radius, the averages in Eq. (5) are $\langle r^n \rangle = (r_{\text{min}}^n + r_{\text{max}}^n)/2$ and the effective radius results,

$$\frac{r_{\text{eff}}}{r_{\text{min}}} = \frac{4}{\left(\frac{r_{\text{min}}}{r_{\text{max}}}\right)^4 + \left(\frac{r_{\text{max}}}{r_{\text{min}}}\right)^3 + \frac{r_{\text{min}}}{r_{\text{max}}} + 1}. \quad (6)$$

This expression clearly shows that the periodically constricted tube yields an effective radius that can be even lower than that of a uniform cylinder of radius r_{min} . Furthermore, for $r_{\text{max}}/r_{\text{min}} \gg 1$, Eq. (6) can be written as follows:

$$\frac{r_{\text{eff}}}{r_{\text{min}}} \approx 4 \left(\frac{r_{\text{min}}}{r_{\text{max}}} \right)^3. \quad (7)$$

The functionality of Eq. (7) suitably captures the characteristic length scales governing the capillary filling of mesoporous materials.⁴⁷ In addition, the trend predicted by Eq. (7) has been experimentally observed in different porous media with bimodal pore size distributions.^{48,49}

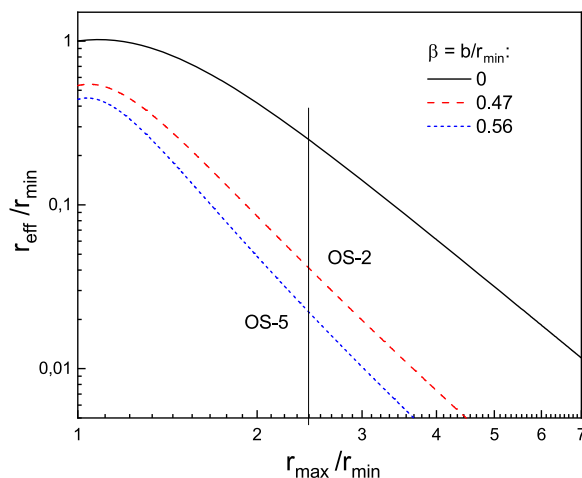


FIG. 3. Theoretical prediction of the effective pore radius (r_{eff}) from Lucas–Washburn dynamics in periodically constricted tubes. The continuous line shows the dependence of r_{eff} with the pore size ratio [$r_{\text{max}}/r_{\text{min}}$, Eq. (6)]. The dashed lines show the model results when an immobile layer of size b is incorporated [Eq. (8)]. Results are shown for two values of b that fit the measured behavior of the oligomers OS-2 and OS-5. The vertical full line stands for the pore ratio (2.43) that characterizes the pSi sample used in the experiments.

If one further considers the presence of an adsorbed layer of polymer, which forms a dead zone of thickness b in the flow field [Fig. 1(e)], then Eq. (6) gives

$$\frac{r_{\text{eff}}}{r_{\text{min}}} = \frac{4(1-\beta)}{\alpha^{-4} + \alpha^3 + \alpha^{-1} + 1}, \quad (8)$$

where $\alpha = [(r_{\text{max}}/r_{\text{min}}) - \beta]/(1 - \beta)$ and $\beta = b/r_{\text{min}}$. Figure 3 illustrates the prediction of Eq. (8), where one readily observes the strong diminution of r_{eff} induced by a uniform layer of stagnant polymer on the pore walls.

In the case of the pSi thin film used in this work (Fig. 1), $\langle r_h \rangle = 5.8$ nm is obtained from the analysis of SEM images.²⁸ Moreover, imbibition measurements with glycerol indicate that this structure has $r_{\text{eff}} \sim 0.9$ nm, which is consistent with a tortuosity of 2.6 [Eq. (4)].²⁸ Then, by combining Eqs. (4), (5), and (7), it is found that the morphology of this layer can be represented considering the model of periodically constricted tubes with $r_{\text{min}} = 3.5$ nm and $r_{\text{max}} = 8.5$ nm, assuming b to be small compared to r_{min} .

In what follows, we derive r_{eff} by fitting the measurements with Eq. (1) and bulk fluid parameters. The thickness b of the immobile layer is subsequently calculated with Eq. (8). In summary, the constriction model describes the imbibition dynamics for different fluids with b as the only free variable.

Figure 4 shows the results obtained for the capillary imbibition of the oligomers. Figure 4(c) shows a contour map of the evolution of spectral reflectance for OS-5. A superimposed dashed line indicates the evolution of the resonance wavelength of the cavity formed by the PC. The first increase in wavelength begins almost immediately and is associated with the arrival of the fluid precursor film to the PC. The second abrupt increase that occurs around 3100 s is associated with the fluid front's arrival to the PC. Figure 4(b) shows in dashed lines the evolution of the microcavity normalized position for measurements carried out with OS-2 and OS-5 in a pSi sample comprised of a thin film that is 9.3 μm thick. The experimental points obtained for the evolution of the stack filling fraction are also included in the same figure. The procedure to determine the time at which the thin film imbibition is completed and the imbibition

of the PC starts (t_{fill}) was the following: First, t_{fill} was determined for OS-5 by identifying the maximum of the second derivative of $\lambda_0(t)$. This filling time was used to normalize the time axis for OS-5 experimental data [$\lambda_0(t)$ and $\lambda_{\text{peak}}(t)$]. Then, the time axis of OS-2 experimental data was normalized with the t_{fill} that best collapses $\lambda_{\text{peak}}(t)$ OS-2 and OS-5 curves. This method is accurate since the compared imbibition experiments were measured in different pieces of the same pSi sample, eliminating any possible morphological variation of the porous structures. It is relevant to note that the filling fraction corresponding to the thin film [indicated with a horizontal dotted line in Fig. 4(b)] effectively occurs in coincidence with the fluid front's arrival at the PC, which is evident by a slope change in $\lambda_0(t)$. Moreover, the filling fraction of 0.8 matches the thickness measured through SEM images.

In Fig. 4(b), a fitting with the Lucas–Washburn [Eq. (1)] equation has been included (solid line) to show that the capillary filling of both oligomers follows the classical \sqrt{t} dynamics in the uniform porosity thin film. The analysis continues by extracting $r_{\text{eff}}^{\text{OS-2}}$ and $r_{\text{eff}}^{\text{OS-5}}$ from Eq. (1) with the corresponding $t = t_{\text{fill}}$ and L equal to the thin film thickness. The obtained results are summarized in Table II. They indicate that $r_{\text{eff}}^{\text{OS-2}}$ and $r_{\text{eff}}^{\text{OS-5}}$ are 5.8 and 11 times smaller than the r_{eff} estimated for glycerol imbibition, respectively. Using Eq. (8), the immobile layer thickness that is consistent with that change in r_{eff} in each case can be estimated. The values obtained in this way are $b_{\text{OS-2}} = 1.6$ nm and $b_{\text{OS-5}} = 1.95$ nm. Quantum mechanical molecular size estimations resulted in 0.9–1.2 nm for OS-2 and 1.4–1.8 nm for OS-5.⁵⁰ The ratio of these sizes of 1.5 is comparable to the ratio of the immobile layer of 1.2. A way to interpret the immobile layer is to consider 1–3 densely packed molecular layers,⁵¹ with molecules stretched in the direction of drag and a slow diffusion at the wall. Note that the existence of such a hydrodynamically dead layer agrees with findings reported on other (simpler) molecular liquids.^{8,52,53}

It is interesting to compare these results with the tortuous pore model [Eq. (4)], which requires $\tau = 6.3$ for OS-2 and $\tau = 8.6$ for OS-5 to predict the above effective radii. Beyond the extremely high values, τ results are different for each measurement, which is not compatible with the fact that the morphology of the thin film is the same in both cases.

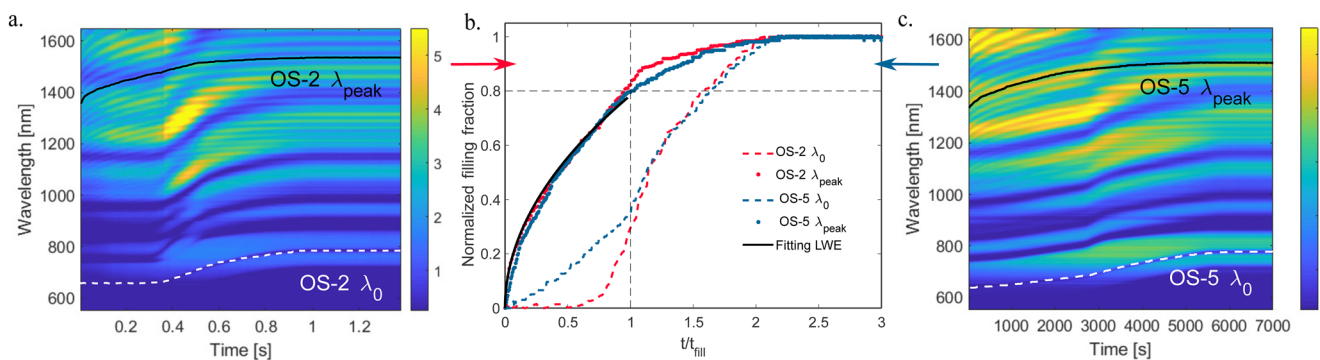


FIG. 4. (a) and (c) Contour plots of the capillary filling of pSi samples for OS-2 and OS-5, respectively. The color scale represents the reflectance intensity in a.u. Solid lines show the evolution of one reflectance peak λ_{peak} during imbibition while dashed lines indicate the evolution of the microcavity position λ_0 . (b) Normalized evolution of λ_{peak} and λ_0 as a function of time normalized with t_{fill} . The solid line shows a fitting with a \sqrt{t} dependence. An equivalent measurement for a different pSi sample can be found in Fig. S1.

TABLE II. Results: The decelerated dynamics in capillary filling can be illustrated by apparent viscosities, μ_{app} , 6- and 11-fold higher than the bulk for OS-2 and OS-5, respectively. In the constriction model, the different capillary rise dynamics of the oligomers is explained by the immobile layer thickness b . The squared fit parameter “ a ” of the main meniscus can be compared to the diffusion-like coefficient D_{PF} of the precursor film spreading. Additionally, a thickness d_{PF} for the precursor film is derived.

| | μ_{app} (mPa s) | b (nm) | a^2 (m ² /s) | D_{PF} (m ² /s) | d_{PF} (nm) |
|------|-------------------------------|-------------|------------------------------|--|-------------------------|
| OS-2 | 54 | 1.60 | 3.3×10^{-10} | ... | ... |
| OS-5 | 3.7×10^5 | 1.95 | 5.1×10^{-14} | 9.4×10^{-13} | 0.9 |

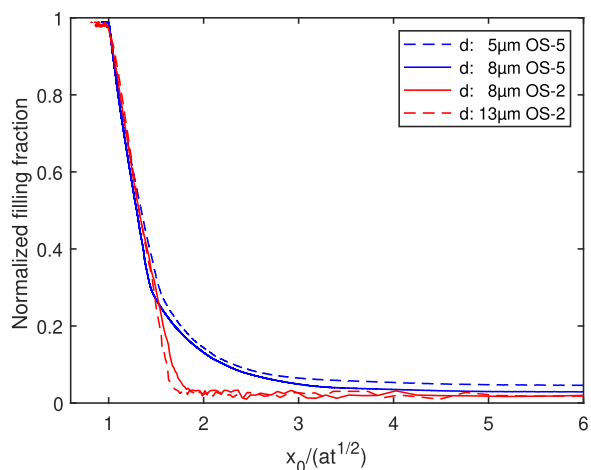


FIG. 5. Fluid front shapes: Filling fraction of the photonic crystal with OS-2 and OS-5 vs a spatiotemporal rescaled variable. “ a ” is the prefactor of a square-root-of-time fit of the filling dynamics of the thin film in front of the PC. The filling time t of the PC is rescaled with respect to its central position x_0 , which is adjusted for the same starting positions of menisci of the respective oligomer. The thickness d in the legend belongs to the pSi layer in front of the PC. It is measured by SEM.

Figure 5 displays the fluid front shapes of OS-2 and OS-5 for two samples each, with different porous layer thicknesses in front of their PC. Thinking in the chronological sequence in the experiment, the figure must be read from right to left, since it has been rescaled in space and time by $x_0/(a\sqrt{t})$. Here, x_0 stands for the middle of the PC and “ a ” is the measured coefficient for capillary rise in the preceding thin film. We calculated x_0 for the abscissa position of one, by the point in time where the filling fraction is converging to a value of one. It can be noted that the fluid front shape for the individual oligomers maintains its shape independent of the thin film layer thickness. OS-2 shows a sharp front, whereas OS-5 has a broad slope, i.e., a precursor film, starting at a value x_{PF} around 4.3 of the abscissa. The onset of the precursor film is determined by the intercept of a linear fit of the constant initial region and the tangent where the filling fraction starts to increase.

A diffusion-like coefficient for the precursor film spreading can be derived using the expression $D_{\text{PF}} = (\tau a x_{\text{PF}})^2$. For the experiments displayed in Fig. 5, a mean of 9.4×10^{-13} m²/s is obtained. Similar to MD simulations on nanopores,¹⁷ the spreading dynamics

of the precursor film follows a faster \sqrt{t} -law than the main meniscus, as can be seen by comparing the squared prefactor of the capillary rise in Table II. The value for the main meniscus of OS-5 is about twenty times smaller than its precursor film, which in turn is more than two orders of magnitude smaller than the capillary rise of OS-2. The latter explains why there is no precursor film observed for OS-2, even if one assumes a faster precursor film formation for this shorter oligomer. If one assumes that D_{PF} scales similarly as a function of the degree of polymerization N as in polymer surface diffusion, where the authors of the work of Sukhishvili *et al.* found a proportionality of $D \sim N^{-3/2}$, there is barely any increase in D_{PF} expected for OS-2 compared to OS-5.⁵⁴ The end of the precursor film region is determined by deviation from a linear fit of the meniscus region by more than the standard deviation in ten consecutive points. Taking the difference of the filling fraction limiting the precursor region, its maximal filling fraction Φ_{PF} can be assessed. A simple tube filling model starting from the pore wall leads to an approximation of the precursor thickness by $\Phi_{\text{PF}} = \frac{2(r_h)d_{\text{PF}} - d_{\text{PF}}^2}{(r_h)^2}$, resulting in $d_{\text{PF}} \approx 0.9$ nm.

VII. CONCLUSION

The combined thin film interference and photonic crystal analysis of pSi during liquid imbibition allows the detection of capillary rise and precursor film dynamics in the same experiment. Especially for polymeric liquids, the necessity to measure capillary rise directly becomes clear, as they exhibit different fluid dynamics when the pore size of the scaffold becomes comparable to the molecule size. In the experiments performed with OS-2 and OS-5, a strong slowdown was observed. This can be explained by an apparent viscosity of about six and eleven times the bulk value, respectively. We, however, explain this by the increasing importance of local undulations in the pore radius with the infiltrating liquid’s molecular size but otherwise unchanged bulk fluid parameters. Indeed, a simplified constriction model with a dead zone consistently describes imbibition in the pSi thin films for both oligomers. This model is superior to the concept of a modified LWE with a tortuosity in terms of having a consistent geometrical description. Moreover, the tortuosity values were found to be unreasonably high, suggesting much more meandering pores than can be deduced from SEM images.

In the present study, the constriction model gives a very good description of the capillary rise dynamics. Even in the framework of the semi-continuum approach, the model relates the measured (macroscopic) variables to parameters that characterize the most important nanoscale features, namely the thickness of the hydrodynamic dead zone. Furthermore, the predicted values are in reasonable agreement with estimates of the molecular size of oligomers.

Following the resonance wavelength of the PC, filling phenomena can be resolved with sub-nanometer precision, enabling the determination of the precursor film’s thickness, which was found to be 0.9 nm for OS-5. The coefficient of capillary rise dynamics determined in the same experiment is used to visualize the shape of the fluid front. For OS-2, the fluid front is flat, while for OS-5 a precursor film is detected. We attribute this to the fact that the pore-surface diffusion dynamics in OS-5 are fast enough to allow a thin film to move beyond the main capillary front. In contrast, the fast imbibition rate of OS-2 precludes precursor film formation. We also

show that our opto-fluidic technique allows to measure the maximum thickness and a surface diffusion-like coefficient of the OS-5 precursor film with remarkably high spatiotemporal resolution.

From an application point of view, the parameters obtained by the method presented could be used to rationally design polymer nanotubes by melt infiltration. Moreover, we envision that our experimental platform can be employed to determine the surface diffusion coefficients of polymers, which is generally a challenging task.

SUPPLEMENTARY MATERIAL

The supplementary material contains two figures. A data set of a different sample is provided in the same manner as in Fig. 4. Additionally, a figure comparing the direct peak fitting and fast Fourier transform method for evaluation of interference patterns is displayed.

ACKNOWLEDGMENTS

The authors acknowledge the funding support received from the following institutions: Deutsche Forschungsgemeinschaft (DFG, German Research Foundation) Project No. 519853330, CRC 986 “Tailor-Made Multi-Scale Materials Systems” Project No. 192346071, “Dynamic Electrowetting at Nanoporous Surfaces: Switchable Spreading, Imbibition, and Elastocapillarity,” Project No. 422879465 (SPP 2171), Consejo Nacional de Investigaciones Científicas y Técnicas, Grant No. PIP-2020-1049, Universidad Nacional del Litoral, Grant No. CAID 2020-50620190100114L.

AUTHOR DECLARATIONS

Conflict of Interest

The authors have no conflicts to disclose.

Author Contributions

Guido Dittrich: Conceptualization (equal); Formal analysis (equal); Investigation (lead); Methodology (equal); Validation (equal); Visualization (equal); Writing – original draft (lead); Writing – review & editing (equal). **Luisa G. Cencha:** Conceptualization (equal); Methodology (equal); Validation (equal); Visualization (equal); Writing – original draft (equal); Writing – review & editing (equal). **Martin Steinhart:** Conceptualization (supporting); Funding acquisition (equal); Investigation (equal); Writing – original draft (equal); Writing – review & editing (equal). **Ralf B. Wehrspohn:** Conceptualization (equal); Funding acquisition (equal); Writing – review & editing (equal). **Claudio L. A. Berli:** Conceptualization (equal); Formal analysis (equal); Validation (equal); Visualization (equal); Writing – original draft (equal); Writing – review & editing (equal). **Raul Urteaga:** Conceptualization (equal); Investigation (equal); Methodology (equal); Validation (equal); Visualization (equal); Writing – original draft (equal); Writing – review & editing (equal). **Patrick Huber:** Conceptualization (equal); Formal analysis (equal); Funding acquisition (equal);

Investigation (equal); Project administration (equal); Supervision (equal); Visualization (equal); Writing – original draft (equal); Writing – review & editing (lead).

DATA AVAILABILITY

The data that support the findings of this study are available from the corresponding author upon reasonable request.

REFERENCES

- ¹M. Krutyeva, A. Wischniewski, M. Monkenbusch, L. Willner, J. Maiz, C. Mijangos, A. Arbe, J. Colmenero, A. Radulescu, O. Holderer, M. Ohl, and D. Richter, “Effect of nanoconfinement on polymer dynamics: Surface layers and interphases,” *Phys. Rev. Lett.* **110**, 108303 (2013).
- ²A. Kusmin, S. Gruener, A. Henschel, O. Holderer, J. Allgaier, D. Richter, and P. Huber, “Evidence of a sticky boundary layer in nanochannels: A neutron spin echo study of *n*-hexatriacontane and poly(ethylene oxide) confined in porous silicon,” *J. Phys. Chem. Lett.* **1**, 3116–3121 (2010).
- ³M. Steinhart, J. H. Wendorff, A. Greiner, R. B. Wehrspohn, K. Nielsch, J. Schilling, J. Choi, and U. Gösele, “Polymer nanotubes by wetting of ordered porous templates,” *Science* **296**, 1997 (2002).
- ⁴L. G. Cencha, G. F. García, N. Budini, R. Urteaga, and C. L. Berli, “Time-temperature indicator based on the variation of the optical response of photonic crystals upon polymer infiltration,” *Sens. Actuators, A* **341**, 113571 (2022).
- ⁵R. Lucas, “Ueber das Zeitgesetz des kapillaren Aufstiegs von Flüssigkeiten,” *Kolloid-Z.* **23**, 15 (1918).
- ⁶E. W. Washburn, “The dynamics of capillary flow,” *Phys. Rev.* **17**, 273 (1921).
- ⁷M. Reyssat, L. Courbin, E. Reyssat, and H. A. Stone, “Imbibition in geometries with axial variations,” *J. Fluid Mech.* **615**, 335 (2008).
- ⁸S. Gruener, T. Hofmann, D. Wallacher, A. V. Kityk, and P. Huber, “Capillary rise of water in hydrophilic nanopores,” *Phys. Rev. E* **79**, 067301 (2009).
- ⁹S. Gruener, H. E. Hermes, B. Schilling, S. U. Egelhaaf, and P. Huber, “Capillary rise dynamics of liquid hydrocarbons in mesoporous silica as explored by gravimetry, optical and neutron imaging: Nano-rheology and determination of pore size distributions from the shape of imbibition fronts,” *Colloids Surf., A* **496**, 13–27 (2016).
- ¹⁰P. Huber, “Soft matter in hard confinement: Phase transition thermodynamics, structure, texture, diffusion and flow in nanoporous media,” *J. Phys.: Condens. Matter* **27**, 103102 (2015).
- ¹¹F. Vazquez Luna, M. Gerstenberger, G. Dittrich, J. M. de Souza e Silva, P. Huber, R. Wehrspohn, and M. Steinhart, “Statistical analysis of submicron x-ray tomography data on polymer imbibition into arrays of cylindrical nanopores,” *J. Phys. Chem. C* **125**, 26731–26743 (2021).
- ¹²F. V. Luna, A. K. Maurya, J. M. de Souza e Silva, G. Dittrich, T. Paul, D. Enke, P. Huber, R. Wehrspohn, and M. Steinhart, “Straight versus spongy: Effect of tortuosity on polymer imbibition into nanoporous matrices assessed by segmentation-free analysis of 3D sample reconstructions,” *J. Phys. Chem. C* **126**, 12765 (2022).
- ¹³L. G. L. Cencha, P. Huber, M. Kappl, G. Floudas, M. Steinhart, C. L. A. Berli, and R. Urteaga, “Nondestructive high-throughput screening of nanopore geometry in porous membranes by imbibition,” *Appl. Phys. Lett.* **115**, 113701 (2019).
- ¹⁴Y. Yao, S. Alexandris, F. Henrich, G. Auernhammer, M. Steinhart, H.-J. Butt, and G. Floudas, “Complex dynamics of capillary imbibition of poly(ethylene oxide) melts in nanoporous alumina,” *J. Chem. Phys.* **146**, 203320 (2017).
- ¹⁵Y. Yao, H.-J. Butt, G. Floudas, J. Zhou, and M. Doi, “Theory on capillary filling of polymer melts in nanopores,” *Macromol. Rapid Commun.* **39**, 1800087 (2018).
- ¹⁶D. Dimitrov, A. Milchev, and K. Binder, “Capillary rise in nanopores: Molecular dynamics evidence for the Lucas–Washburn equation,” *Phys. Rev. Lett.* **99**, 054501 (2007).
- ¹⁷S. Chibbaro, L. Biferale, F. Diotallevi, S. Succi, K. Binder, D. Dimitrov, A. Milchev, S. Girardo, and D. Pisignano, “Evidence of thin-film precursors formation in hydrokinetic and atomistic simulations of nano-channel capillary filling,” *Europhys. Lett.* **84**, 44003 (2008).

- ¹⁸M. Engel and B. Stühn, “*In situ* small angle x-ray scattering measurements of the filling process of polyisobutylene and poly- ϵ -caprolactone in ion track etched polycarbonate nanopores,” *J. Chem. Phys.* **132**, 224502 (2010).
- ¹⁹C.-H. Tu, J. Zhou, M. Doi, H.-J. Butt, and G. Floudas, “Interfacial interactions during *in situ* polymer imbibition in nanopores,” *Phys. Rev. Lett.* **125**, 127802 (2020).
- ²⁰J. Zhang, J. Lei, W. Tian, G. Zhang, G. Floudas, and J. Zhou, “Capillary filling of polymer chains in nanopores,” *Macromolecules* **56**, 2258–2267 (2023).
- ²¹M. J. Sailor, *Porous Silicon in Practice* (John Wiley & Sons, 2012).
- ²²L. T. Canham, in *Handbook of Porous Silicon*, edited by L. Canham (Springer, 2015).
- ²³M. Brinker, G. Dittrich, C. Richert, P. Lakner, T. Krekeler, T. F. Keller, N. Huber, and P. Huber, “Giant electrochemical actuation in a nanoporous silicon-polyppyrrrole hybrid material,” *Sci. Adv.* **6**, eaba1483 (2020).
- ²⁴M. Brinker and P. Huber, “Wafer-scale electroactive nanoporous silicon: Large and fully reversible electrochemo-mechanical actuation in aqueous electrolytes,” *Adv. Mater.* **34**, 2105923 (2022).
- ²⁵M. Brinker, M. Thelen, M. May, D. Rings, T. Krekeler, P. Lakner, T. F. Keller, F. Bertram, N. Huber, and P. Huber, “How nanoporous silicon-polyppyrrrole hybrids flex their muscles in aqueous electrolytes: In operando high-resolution x-ray diffraction and electron tomography-based micromechanical computer simulations,” *Phys. Rev. Mater.* **6**, 116002 (2022).
- ²⁶C. Pacholski, “Photonic crystal sensors based on porous silicon,” *Sensors* **13**, 4694–4713 (2013).
- ²⁷H. Lin, T. Gao, J. Fantini, and M. J. Sailor, “A porous silicon–palladium composite film for optical interferometric sensing of hydrogen,” *Langmuir* **20**, 5104–5108 (2004).
- ²⁸L. G. Cench, G. Dittrich, P. Huber, C. L. Berli, and R. Urteaga, “Precursor film spreading during liquid imbibition in nanoporous photonic crystals,” *Phys. Rev. Lett.* **125**, 234502 (2020).
- ²⁹A. Henschel, T. Hofmann, P. Huber, and K. Knorr, “Preferred orientations and stability of medium length *n*-alkanes solidified in mesoporous silicon,” *Phys. Rev. E* **75**, 021607 (2007).
- ³⁰T. Hofmann, D. Wallacher, M. Mayorova, R. Zorn, B. Frick, and P. Huber, “Molecular dynamics of *n*-hexane: A quasi-elastic neutron scattering study on the bulk and spatially nanochannel-confined liquid,” *J. Chem. Phys.* **136**, 124505 (2012).
- ³¹S. Calus, D. Rau, P. Huber, A. V. Kityk, S. Calus, D. Rau, P. Huber, A. V. Kityk, and S. Calus, “Influence of nanoconfinement on the nematic behavior of liquid crystals,” *Phys. Rev. E* **86**, 021701 (2012).
- ³²D. Kondrashova, A. Lauerer, D. Mehlhorn, H. Jobic, A. Feldhoff, M. Thommes, D. Chakraborty, C. Gommès, J. Zecevic, P. de Jongh, A. Bunde, J. Kärger, and R. Valiullin, “Scale-dependent diffusion anisotropy in nanoporous silicon,” *Sci. Rep.* **7**, 40207 (2017).
- ³³G. Y. Gor, L. Bertinetti, N. Bernstein, T. Hofmann, P. Fratzl, and P. Huber, “Elastic response of mesoporous silicon to capillary pressures in the pores,” *Appl. Phys. Lett.* **106**, 261901 (2015).
- ³⁴M. Thelen, N. Bochud, M. Brinker, C. Prada, and P. Huber, “Laser-excited elastic guided waves reveal the complex mechanics of nanoporous silicon,” *Nat. Commun.* **12**, 3597 (2021).
- ³⁵B.-Y. Cao, M. Yang, and G.-J. Hu, “Capillary filling dynamics of polymer melts in nanopores: Experiments and rheological modelling,” *RSC Adv.* **6**, 7553–7559 (2016).
- ³⁶S. Wu, “Surface and interfacial tensions of polymer melts. II. Poly(methyl methacrylate), poly(*n*-butyl methacrylate), and polystyrene,” *J. Phys. Chem.* **74**, 632–638 (1970).
- ³⁷W. Xu, K. Mihhels, N. Kotov, S. Lepikko, R. H. Ras, C. M. Johnson, T. Pettersson, and E. Kontturi, “Solid-state polymer adsorption for surface modification: The role of molecular weight,” *J. Colloid Interface Sci.* **605**, 441–450 (2022).
- ³⁸M. A. Green, “Self-consistent optical parameters of intrinsic silicon at 300 K including temperature coefficients,” *Sol. Energy Mater. Sol. Cells* **92**, 1305–1310 (2008).
- ³⁹E. R. Peck and K. Reeder, “Dispersion of air,” *J. Opt. Soc. Am.* **62**, 958–962 (1972).
- ⁴⁰X. Zhang, J. Qiu, X. Li, J. Zhao, and L. Liu, “Complex refractive indices measurements of polymers in visible and near-infrared bands,” *Appl. Opt.* **59**, 2337–2344 (2020).
- ⁴¹L. N. Acquaroli, R. Urteaga, C. L. Berli, and R. R. Koropecski, “Capillary filling in nanostructured porous silicon,” *Langmuir* **27**, 2067–2072 (2011).
- ⁴²D. Jalas, R. Canchi, A. Y. Petrov, S. Lang, L. Shao, J. Weissmüller, and M. Eich, “Effective medium model for the spectral properties of nanoporous gold in the visible,” *Appl. Phys. Lett.* **105**, 241906 (2014).
- ⁴³L. G. Cench, R. Urteaga, and C. L. Berli, “Interferometric technique to determine the dynamics of polymeric fluids under strong confinement,” *Macromolecules* **51**, 8721–8728 (2018).
- ⁴⁴N. Kavokine, R. R. Netz, and L. Bocquet, “Fluids at the nanoscale: From continuum to subcontinuum transport,” *Annu. Rev. Fluid Mech.* **53**, 377–410 (2021).
- ⁴⁵N. Franck, C. L. A. Berli, P. A. Kler, and R. Urteaga, “Multiphysics approach for fluid and charge transport in paper-based microfluidics,” *Microfluid. Nanofluid.* **26**, 87 (2022).
- ⁴⁶R. Sharma and D. S. Ross, “Kinetics of liquid penetration into periodically constricted capillaries,” *J. Chem. Soc., Faraday Trans.* **87**, 619 (1991).
- ⁴⁷C. L. A. Berli, M. Mercuri, and M. G. Bellino, “Modeling the abnormally slow infiltration rate in mesoporous films,” *Phys. Chem. Chem. Phys.* **19**, 1731–1734 (2017).
- ⁴⁸F. Dullien, M. El-Sayed, and V. Batra, “Rate of capillary rise in porous media with nonuniform pores,” *J. Colloid Interface Sci.* **60**, 497–506 (1977).
- ⁴⁹D. Patro, S. Bhattacharyya, and V. Jayaram, “Flow kinetics in porous ceramics: Understanding with non-uniform capillary models,” *J. Am. Ceram. Soc.* **90**, 3040–3046 (2007).
- ⁵⁰J. H. Jensen and J. C. Kromann, “The molecule calculator: A web application for fast quantum mechanics-based estimation of molecular properties,” *J. Chem. Educ.* **90**, 1093 (2013).
- ⁵¹Y. Zhang, C. Fowler, J. Liang, B. Azhar, M. Y. Shalaginov, S. Deckoff-Jones, S. An, J. B. Chou, C. M. Roberts, V. Liberman, M. Kang, C. Ríos, K. A. Richardson, C. Rivero-Baleine, T. Gu, H. Zhang, and J. Hu, “Electrically reconfigurable non-volatile metasurface using low-loss optical phase-change material,” *Nat. Nanotechnol.* **16**, 661–666 (2021).
- ⁵²O. Vincent, A. Szenicer, and A. D. Stroock, “Capillarity-driven flows at the continuum limit,” *Soft Matter* **12**, 6656–6661 (2016).
- ⁵³S. Gruener and P. Huber, “Capillarity-driven oil flow in nanopores: Darcy scale analysis of Lucas–Washburn imbibition dynamics,” *Transp. Porous Media* **126**, 599–614 (2019).
- ⁵⁴S. A. Sukhishvili, Y. Chen, J. D. Müller, E. Gratton, K. S. Schweizer, and S. Granick, “Surface diffusion of poly(ethylene glycol),” *Macromolecules* **35**, 1776–1784 (2002).